Ocean Modelling 70 (2013) 207–220

Contents lists available at SciVerse ScienceDirect

Ocean Modelling

journal homepage: www.elsevier.com/locate/ocemod

Patterns and cycles in the Climate Forecast System Reanalysis wind and wave data

Justin E. Stopa [a,1], Kwok Fai Cheung [a,*], Hendrik L. Tolman [b,2], Arun Chawla [b,3]

[a] Department of Ocean and Resources Engineering, University of Hawaii at Manoa (ORE-UHM), Honolulu, HI 96822, USA
[b] National Oceanic and Atmospheric Administration, National Centers for Environmental Prediction, Environmental Modeling Center (NOAA-NCEP-EMC), College Park, MD 20740, USA

ARTICLE INFO

Article history:
Available online 10 November 2012

Keywords:
Climate Forecast System Reanalysis
Wave modeling
Climate cycles
Wave hindcasting
WAVEWATCH III

ABSTRACT

The Climate Forecast System Reanalysis and the corresponding WAVEWATCH III hindcast datasets allow climatic interpretation of winds as well as their impacts on waves. In this paper, we analyze the continuous 31 years of global wind and wave data in terms of climate patterns and cycles. Quarterly averages and percentile plots of the wind speed and wave height illustrate the seasonal pattern and distributions of extreme events, while the annual and inter-annual variability demonstrates the wind and wave climate. The data is correlated with published indices of known atmospheric cycles. The datasets show good correspondence with the Arctic Oscillation, Antarctic Oscillation, El Nino Southern Oscillation, and the Madden-Julian Oscillation in both the wind and wave fields. The results compare well with published climate studies on regional scales and provide important linkage to the global wave climate characteristics.

Published by Elsevier Ltd.

1. Introduction

Wave climate has assumed greater importance in the daily utilization of ocean resources for commerce and recreation as well as long-term planning for coastal land-use and hazard mitigation. Winds transfer momentum to the ocean providing the energy source for seas and swells, and as the atmospheric climate evolves so does the wave climate. It is therefore necessary to analyze surface winds and waves simultaneously to understand the physical and climatic processes. Datasets of wide coverage and sufficient duration are essential for interpretation of the global phenomena at numerous temporal and spatial scales.

Wind and wave data is available from buoys, voluntary observing ships, satellite altimetry, and numerical models. Buoys provide ground truth for validation of observational and model data. Despite the lack of spatial coverage, buoy data represents a critical source of information for assessment of climate variability (e.g., Bromirski et al., 2005; Menendez et al., 2008; Genmrich et al., 2011). Ship visual observations were shown by Gulev and Grigorieva (2006) as an accurate source of information, but have limited coverage in the Southern Hemisphere and in extreme conditions (Gulev et al., 2003). Numerous studies have used satellite altimetry to describe the wind and wave climate as well as extreme events (e.g., Young, 1999; Woolf et al., 2002; Chen et al., 2002; Hemer et al., 2010; Young et al., 2011; Izaguirre et al., 2011; Vinoth and Young, 2011). Third generation phase-averaged wave models such as WAve Model (WAM) described by WAMDIG (1988) and WAVEWATCH III (WW3) of Tolman et al. (2002) have greatly complemented observational data in terms of resolution and coverage providing new insights into the global wave climate as well as smaller scale processes.

The quality of the wave data from numerical models depends on the wind forcing. Reanalysis datasets, which are based on the best available models and data assimilation techniques, are most suitable for production of wave datasets. The National Centers for Environmental Predictions (NCEP) produced the global Reanalysis I and II (R1 and R2) datasets covering respectively from 1948 and 1979 to the present time at 1.9° resolution every 6 h (Kalnay et al., 1996; Kistler et al., 2001). The European Centre for Medium-Range Weather Forecasts (ECMWF) created the ERA-15 and ERA-40 for 1979–1993 and 1957–2001 at 1.125° available every 6 h (Sterl et al., 1998; Uppala et al., 2005). ERA-40 is a coupled atmosphere-wave model utilizing WAM to produce wave heights, periods, and directions at 1.5° resolution. Sterl and Caires (2005) validated the wave heights and statistically corrected the dataset with measurements to produce a wave atlas. Studies of hindcast wave data have identified relationships between the wave field and atmospheric cycles in the north Atlantic (Wang and Swail, 2001; Dodet et al., 2010), the Pacific Basin (Graham and Diaz, 2001; Tsai et al., 2012), the Southern Ocean (Hemer et al., 2010;

* Corresponding author. Tel.: +1 (808) 956 3485; fax: +1 (808) 956 3498.
E-mail addresses: stopa@hawaii.edu (J.E. Stopa), cheung@hawaii.edu (K.F. Cheung), hendrik.tolman@noaa.gov (H.L. Tolman), arun.chawla@noaa.gov (A. Chawla).
[1] Tel.: +1 (808) 956 8198; fax: +1 (808) 956 3498.
[2] Tel.: +1 (301) 763 8000x7253; fax: +1 (301) 763 8545.
[3] Tel.: +1 (301) 763 8000x7209; fax: +1 (301) 763 8545.

1463-5003/$ - see front matter Published by Elsevier Ltd.
http://dx.doi.org/10.1016/j.ocemod.2012.10.005

Bosserelle et al., 2011), and globally (Semedo et al., 2011; Reguero et al., 2012; Fan et al., 2012).

Newly available reanalysis datasets, such as NCEP's Climate Forecast System Reanalysis (CFSR) for 1979–2009 at 0.34° available every hour and ECMWF's ERA-Interim for 1979-present at ~0.7° available every 3 h, have updated physics and improved assimilation (Saha et al., 2010; Dee et al., 2011). The CFSR and ERA-Interim datasets perform superior to earlier reanalysis datasets developed by NCEP and ECMWF. These datasets provide an opportunity to re-evaluate the global wind and wave climate at much higher fidelity and resolution than before. In particular, the main improvements in CFSR are coupling between ocean, atmosphere, and land surface processes; an interactive sea ice model; assimilation of satellite radiances to provide temperature and moisture profiles; and increased horizontal and vertical resolution in the atmosphere model. NCEP has utilized the CFSR surface winds to create a hindcast wave dataset at 0.5° resolution using WW3 v3.14 for the period 1979–2009 (Chawla et al., 2013). Using the two-way nesting algorithm of Tolman (2008), higher resolution grids as fine as 1/15° are nested into the global wave model to cover semi-enclosed seas and nearshore regions.

The present study provides a systematic analysis of the newly released CFSR wind and WW3 generated wave datasets from NCEP to complement the numerous studies at regional and global scales. The high-resolution data around the globe allows examination of large and small-scales features as well as their relationships with climate cycles. In this paper, we summarize atmospheric climate cycles and illustrate representative signals from the literature in Section 2. This provides the background for the subsequent analysis of the wind and wave climate. Section 3 provides a summary of the methodologies and validation of the CFSR data products from Saha et al. (2010) and Chawla et al. (2013). Data anomalies are pointed out and their effects on the climate analysis are discussed. Section 4 illustrates the seasonal pattern and statistical properties, while Section 5 discusses annual and inter-annual variability of the wind and wave datasets. Section 6 analyzes the variability of the datasets against published indices from atmospheric oscillations. The results from Sections 4–6 are highlighted for discussion in terms of their implications to ocean modeling and the connections to climate cycles. Section 7 gives a summary of the major findings pertinent to climate research and wave modeling communities.

2. Climate cycles

The CFSR provides continuous and consistent coverage of the atmospheric conditions around the globe for 31 years. This allows examination of climate cycles on global and regional scales with periods up to several years. These include the Arctic Oscillation (AO), Antarctic Oscillation (AAO), El Nino Southern Oscillation (ENSO), and Madden-Julian Oscillation (MJO). Longer cycles such as the Pacific Decadal Oscillation (PDO) and the Atlantic Multi-decadal Oscillation (AMO), which have periods of 10 and 65–80 years, are outside the 31-year range and are not considered here. Many researchers have defined indices representative of the AO, AAO, ENSO, and MJO for an independent analysis of the long-term signals contained in the CFSR data products.

Both hemispheres have circulation modes that can explain the majority of the climate variability. Walker and Bliss (1932) were among the first to identify the North Atlantic Oscillation (NAO) as a regional phenomenon and defined the index as the normalized pressure difference between Iceland and Portugal (or the Azores). Wallace and Gutzler (1981) saw the oscillation as a hemispheric phenomenon and subsequently Thompson and Wallace (1998) defined the Arctic Oscillation (AO) as the first mode of the Empirical Orthogonal Function (EOF) analysis of the 1000 mb pressure level pole-ward of 20°N from the R1 dataset. The corresponding Eigenvalue defines the AO index to account for the semi-permanent low-pressure over the pole. The Southern Hemisphere has a similar phenomenon called the Antarctic Oscillation (AAO), which is defined the same way as the AO through the EOF analysis of the 1000 mb pressure level from the R1 dataset. The AO and AAO are also known as the Northern Annular Mode (NAM) and Southern Annular Mode (SAM) respectively. The AO and AAO indices from Thompson and Wallace (1998) are plotted in the left column of Fig. 1 (available: cpc.ncep.noaa.gov/products/precip/CWlink/daily_ao_index/ao_index.html). Both signals have typical periods of 1–2 years albeit with a broad range of frequencies.

In the equatorial region of the Pacific, the Southern Oscillation Index (SOI) is an excellent indicator of the large-scale climate patterns. Walker and Bliss, (1932), (1937) were the first to define this index, which is the normalized atmospheric pressure difference between Tahiti and Darwin, Australia. A positive value resulting from higher pressure in Tahiti represents the La Nina phase, while a negative value represents the El Nino phase. As such, the SOI provides an indicator of the El Nino Southern Oscillation (ENSO) phenomenon. Alexander et al. (2002) linked the Southern Oscillation to the intensity of the extratropical circulation in the Pacific Ocean. The SOI calculated from pressure measurements taken at Tahiti and Darwin is shown in the top right panel of Fig. 1 (cpc.ncep.noaa.gov/products/precip/CWlink/MJO/enso.shtml). The signal shows dominant periods of 2–7 years with a significant amount of high frequency noise. Strong El Nino's occurred in 1983, 1992, 1998, and 2005 and strong La Nina phases occurred in 1988, 1999, and 2008, corroborating the records.

The Madden-Julian Oscillation (MJO) is the strongest intra-seasonal mode affecting the tropics with far-reaching effects on the global weather pattern. The MJO was first discovered by Madden and Julian (1972) through analysis of wind data. Unlike the ENSO phenomenon, the MJO propagates across the tropics. The oscillation, which is usually triggered in the Indian Ocean, can reach as far as the Atlantic via the Pacific. The MJO is typically generated every 30–90 days and the signal propagates at 4–8 m/s across the ocean. Many researchers have attempted to create an appropriate index to measure the propagating MJO. Wheeler and Hendon (2004) used an EOF analysis of the averaged 850 mb zonal winds, 200 mb zonal winds, and the outgoing long wave radiation near the Equator from the R2 dataset. The Eigen-values of the two leading modes provide a quantitative description of the phenomenon (cawcr.gov.au/staff/mwheeler/maproom/RMM/). Their sum, after removing the mean, provides an index for the MJO. The bottom right panel of Fig. 1 shows the data in 2008 as an example. The periodicity is clearly seen on the order of 30–60 days.

3. CFSR data products

CFSR comprises a suite of coupled atmosphere, ocean circulation, land surface, and sea ice models for environmental prediction (Saha et al., 2010). The Global Forecast System (GFS) of Yang et al. (2006) constitutes the atmosphere model, which has ~38 km horizontal resolution and 64 vertical layers extending from the surface to 0.26 hPa. The Geophysical Fluid Dynamic Lab's Modular Ocean Model (MOM) version 4 describes the ocean circulation at 0.25° resolution in the equatorial region and 0.5° above the tropics with 40 levels extending to 4737 m depth. The Noah land model of Ek et al. (2003) includes 4 soil layers and the ice model of Wu et al. (2005) has 2 layers to account for variations below the surface. Other reanalysis datasets, such as R1, R2, ERA-15, and ERA-40, have laid the groundwork and best practice to assemble and convert observations into an internationally agreed upon data format for model assimilation (Kleist et al., 2009). The same model and data

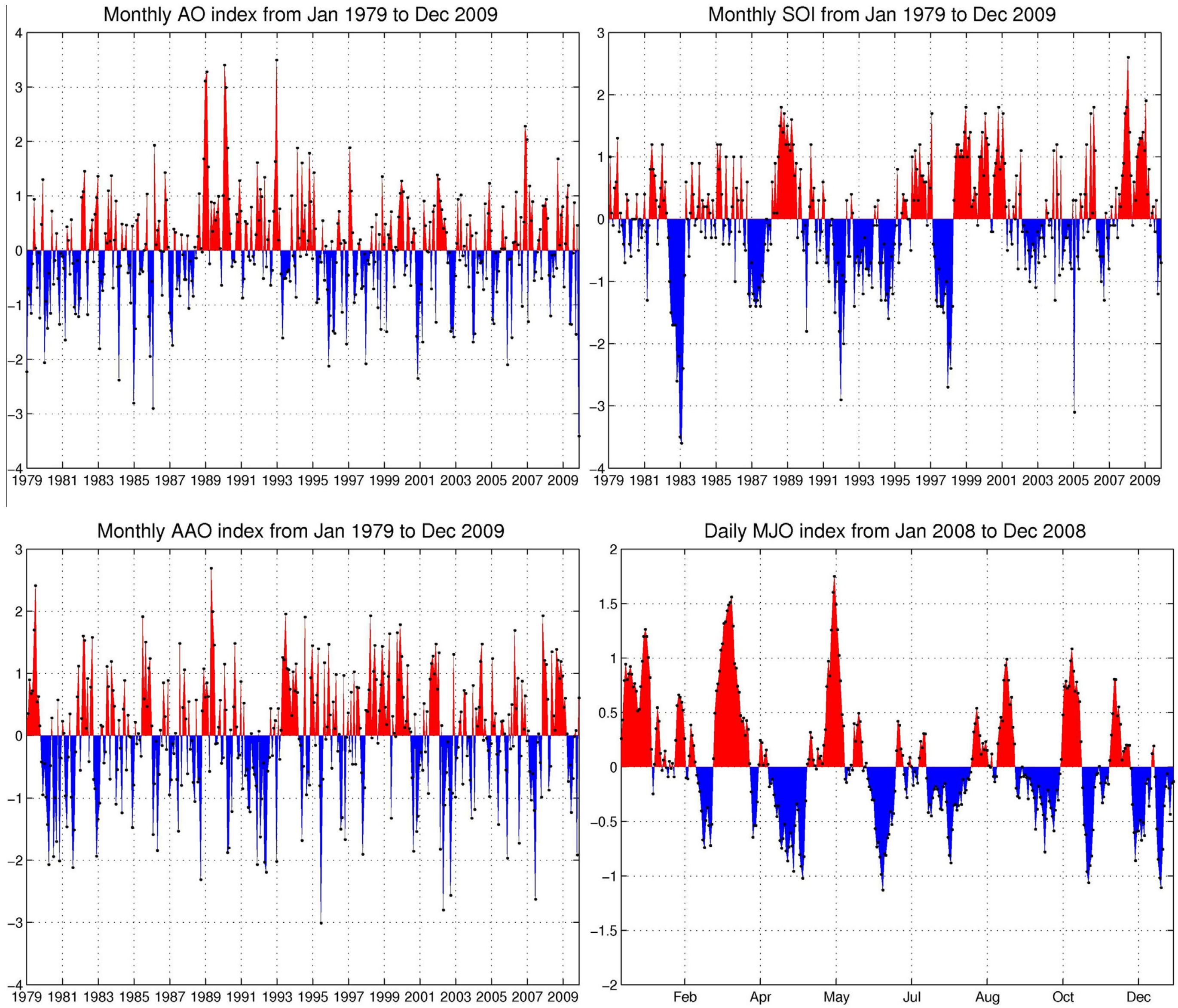

Fig. 1. Published indices of climate cycles.

assimilation techniques were used throughout the reanalysis to provide a consistent dataset. CFSR operates by running a coupled 9-h GFS, MOM, and ice forecast at 0000, 0600, 1200, and 1800 UTC with the excess 3 h accounting for the data window and time derivatives during assimilation of observations into the initial conditions. The land surface model is incorporated at 0000 UTC using observed precipitation from 1800 UTC. The CFSR surface winds (at 10 m elevation) are available hourly at 0.5° resolution for the globe from 1979–2009.

Chawla et al. (2013) described a hindcast study using WW3 forced by 31 years of CFSR winds. The phased averaged model evolves the action density for a range of frequencies over 360° of directions under wind forcing and geographical constraints. The processes are governed by the action balance equation with the source terms accounting for nonlinear effects such as wind-wave interactions, quadruplet wave-wave interactions, and dissipation through whitecapping, bottom friction, and breaking. Hourly surface winds at 10-m elevation along with the temperature difference between the ocean and atmosphere from the CFSR dataset provided the forcing through the source term package from Tolman and Chalikov (1996). Passive microwave sensors aboard the SMMR and SSMI satellites are used to define the daily ice concentrations at 0.5° resolution. WW3 is solved with a finite difference scheme with the computational domain defined by the bathymetry. An obstructions file accounts for sub-grid geographical features, such as smaller islands and atolls (Chawla and Tolman, 2008). The 0.5° gridded output includes the significant wave height, peak period, and peak direction amongst others over the entire globe for the period of 1979–2009 at 3 h intervals.

The CFSR dataset, which already included assimilation of observations, has been verified with previous reanalysis data and validated with independent measurements (Saha et al., 2010). Chawla et al. (2013) evaluated the CFSR wind data using altimeter and buoy measurements prior to its implementation in wave hindcasting. The altimetry wind data, which was not used in the CFSR, allows independent validation of the products. They identified an anomalous feature in the wind distribution in the Southern Hemisphere. The higher percentile wind speed shows a drop around

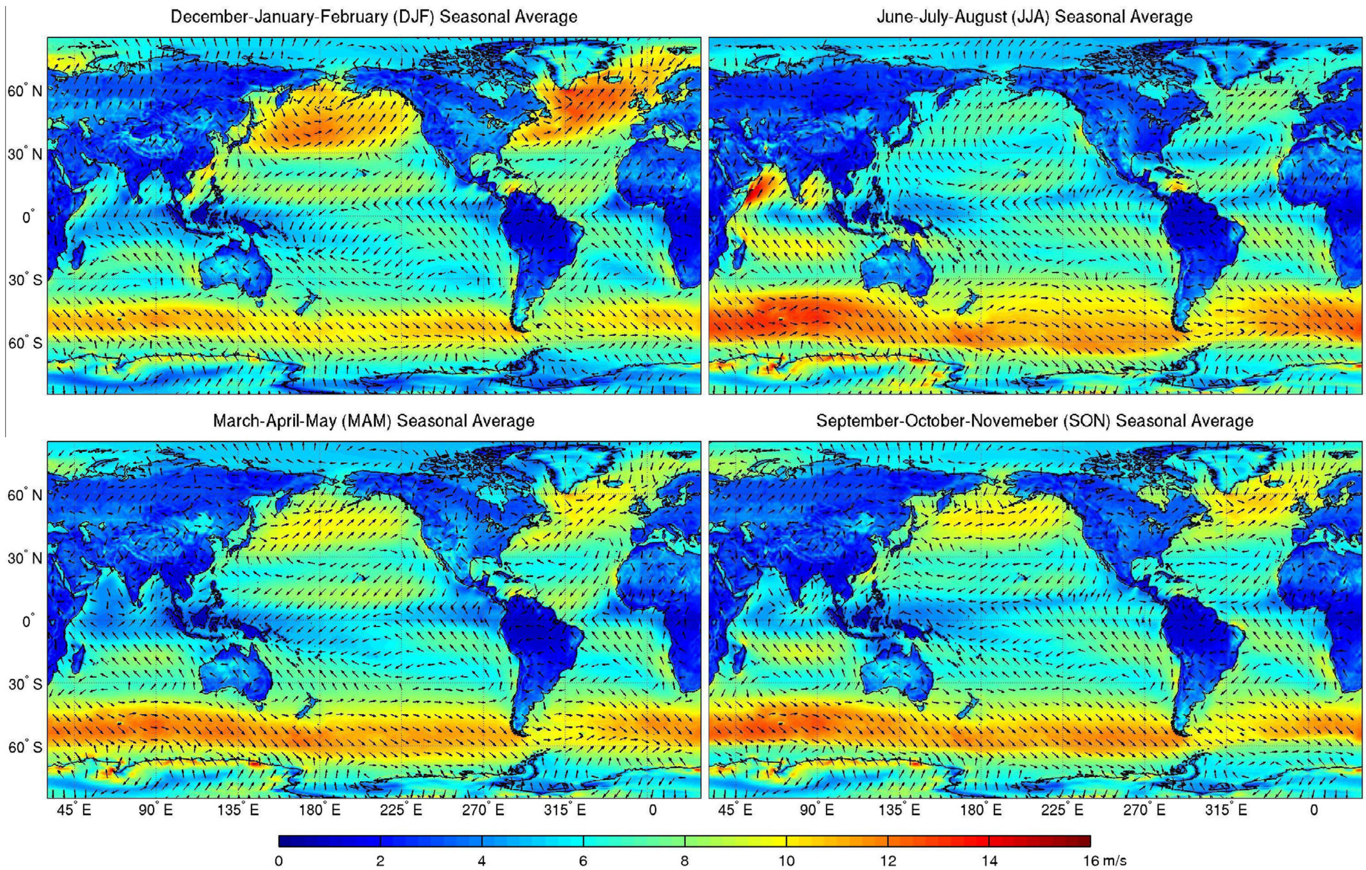

Fig. 2. Seasonal average of wind speed and direction.

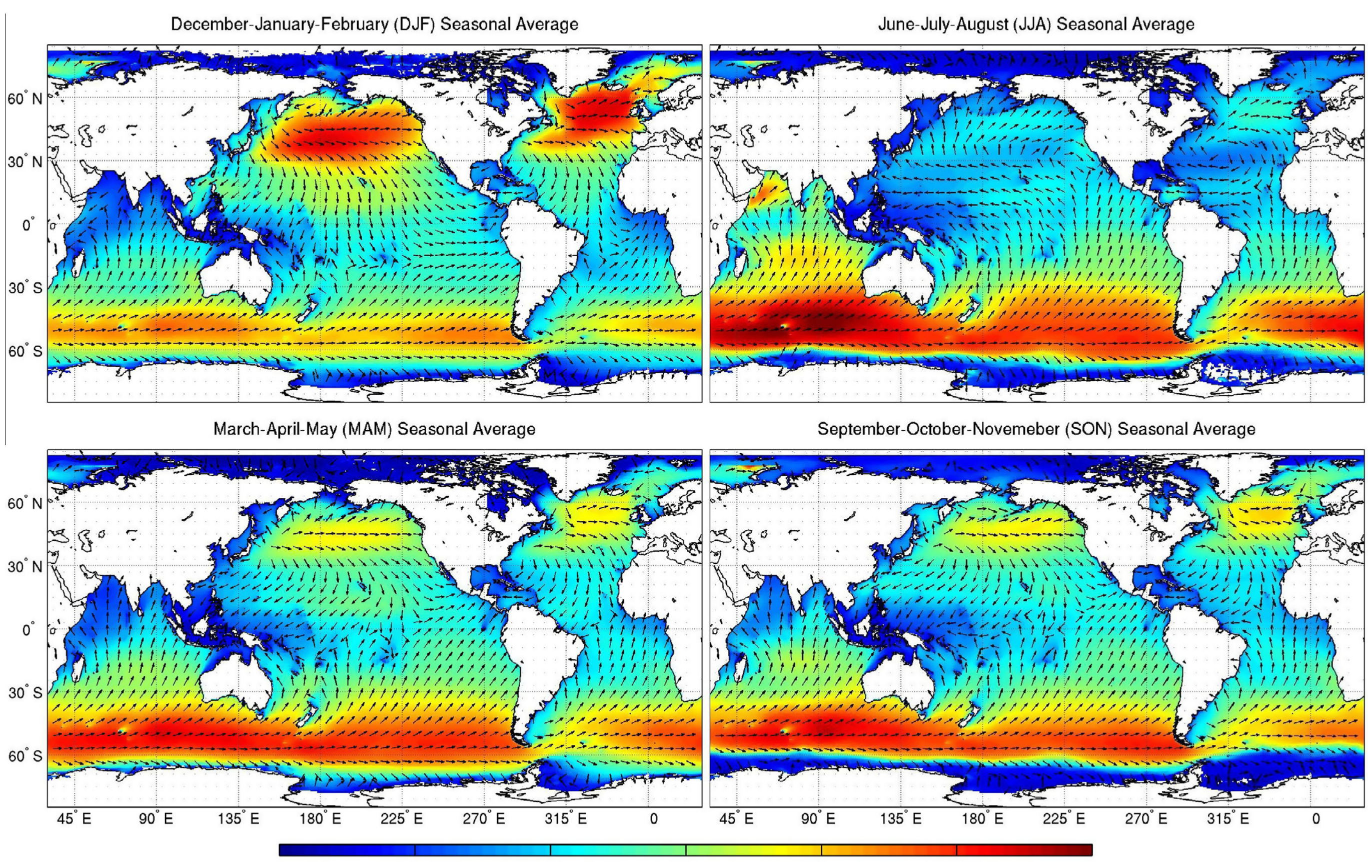

Fig. 3. Seasonal average of significant wave height and peak direction.

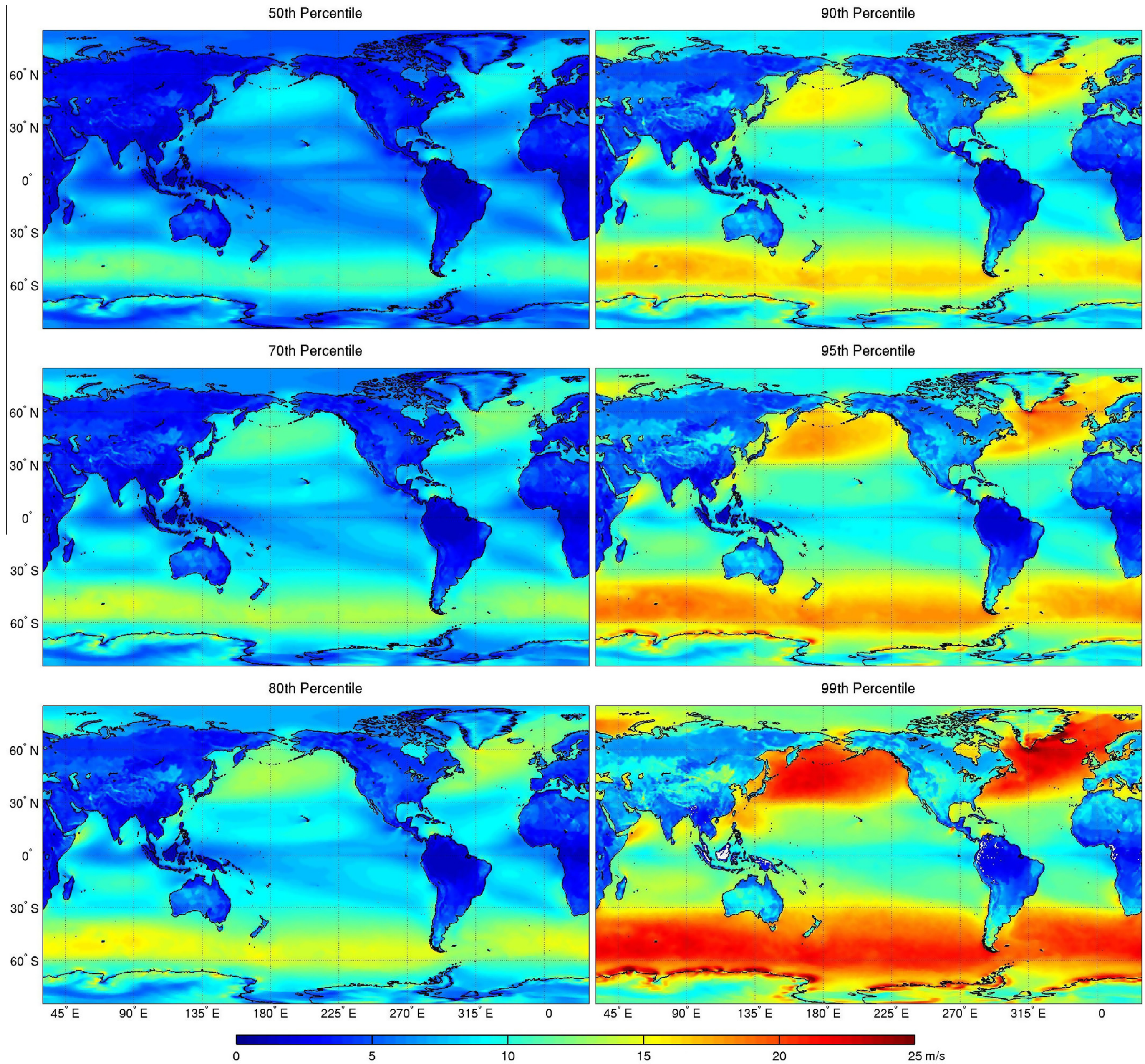

Fig. 4. Wind speed percentiles.

1993–1994 that appears to correspond with the introduction of the SSM-I data in the assimilation. Comparisons with altimetry data show that prior to 1993–1994, the higher percentile wind speed was over predicted in CFSR by about 10%. A second small discontinuity in the higher percentile wind speed in the Southern Hemisphere was observed in 2006. Since wave dynamics represent a non-linear process in which the stronger winds play a much more significant role, these shifts will affect the overall trend of the wave data, but should not have significant effects on the scale of the shorter climate cycles considered here. Despite these shifts, Chawla et al. (2013) showed that the comparisons of the wind and wave data with measurements are excellent with correlation coefficients on the order of 0.9. Quantile comparisons with buoy data show excellent agreement up to the 99.9th percentile. The error metrics compare very well against other reanalysis driven wave datasets (e.g., Caires et al., 2004).

The high temporal and spatial resolution of the CFS data products allows for the analysis of large and small scale physical phenomena and their cycles. We first examine the seasonal patterns from the quarterly average wind speed and significant wave height. This provides the basis for interpretation of the statistical distributions, annual variability, and inter-annual variability of the data. The monthly time series of the AO index, AAO index, and SOI in Fig. 1 are used in the analysis of the cycles of the data. Monthly averages of the highest 10% of the wind speed and wave height are used to give an estimate of how the oscillations affect the wind and wave intensity. In addition, the monthly occurrence of the severe events defined as record counts above the 90th percentile for each grid point is compared to the signals. The MJO index has much smaller periods. Its daily values are compared to daily averages of the wind speed and wave height. Correlation coefficients are computed for each cycle indicating the strength of the relationship.

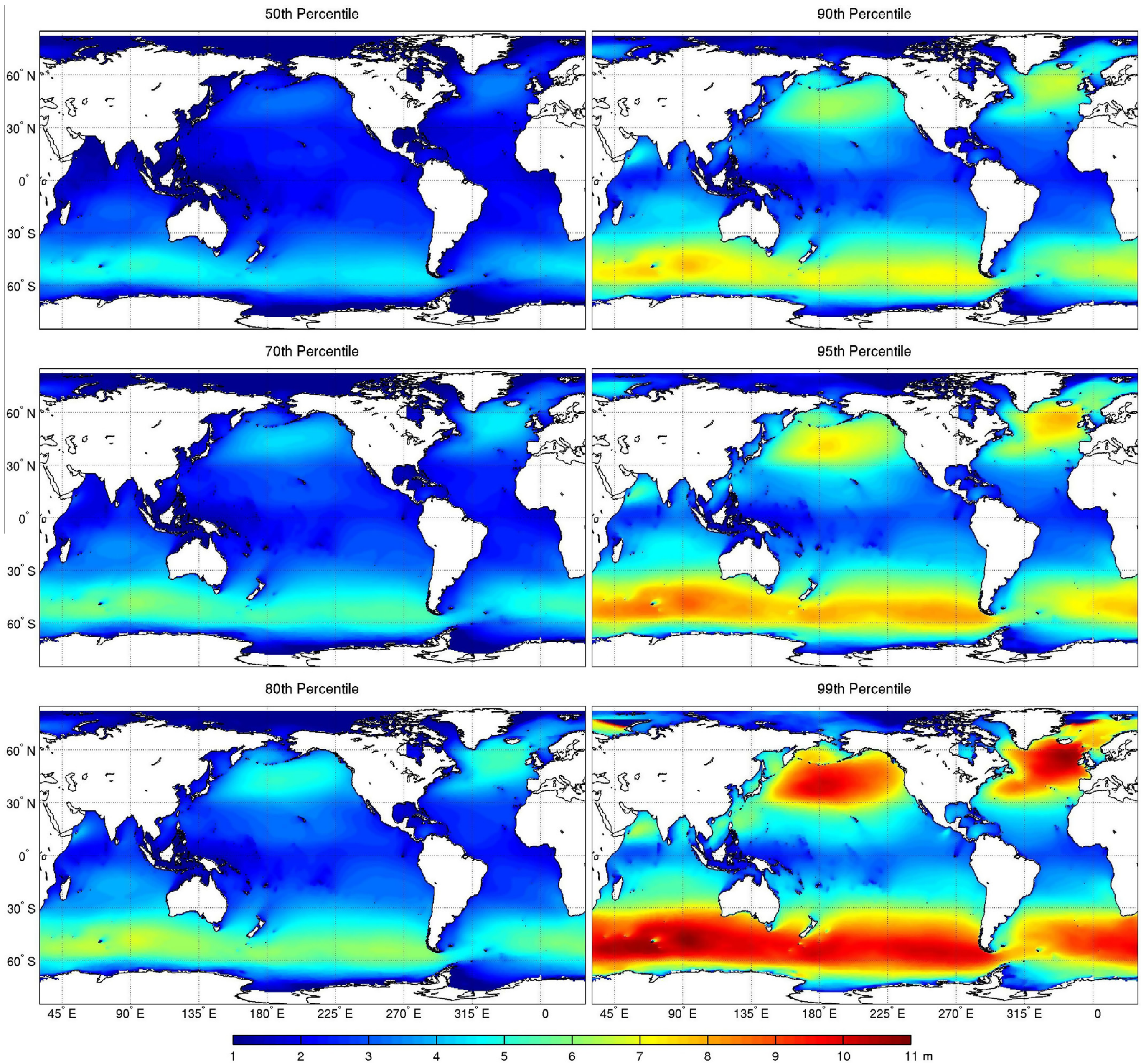

Fig. 5. Significant wave height percentiles.

4. Seasonal patterns and statistics

Seasonal patterns are described by averaging the wind speed and significant wave height in the four quarters: December–January–February (DJF), March–April–May (MAM), June–July–August (JJA), and September–October–November (SON). Figs. 2 and 3 show the respective seasonal averages from the 31 years of data. The directional arrows for the wind speed are computed from the two orthogonal components, while the directional arrows for the significant wave height present the average peak direction. DJF sees extended areas of large wind speed and wave height in the north Pacific and north Atlantic around 50°N, while the activity in the south is at its lowest level confined to a relatively narrow band along 50°S. Although the swells from the north Pacific spread across most of the basin, a swell front developed in the Southern Ocean extends from New Zealand to Central America (Young, 1999). In MAM, the wind and wave activities in the north Pacific and north Atlantic weaken and retreat to upper latitudes. In the Southern Hemisphere, the strongest winds and waves extend toward the Equator encompassing a larger geographical region. JJA has minimal wind and wave activities in the Northern Hemisphere, while the activities in the Southern Hemisphere reach their peaks. Swells generated near Antarctic dominate the Indian and Pacific Oceans. SON is similar to MAM that serves as transition between JJA and DJF and thus has characteristics of both seasons.

The seasonally averaged wind speed and wave height clearly show the zonal pattern of the global circulation with the most prominent features being the Westerlies in 30°–60°, the trade wind belts in 8°–30°, and calm wind and waves near the Equator. The Westerlies in the north Pacific and north Atlantic show seasonal extremes, while the Westerlies in the Southern Hemisphere are more consistent throughout the year. The trade wind regions of both hemispheres have lower intra-annual variability. Analysis of the hindcast data has shown stronger trade winds in the Northern

Hemisphere with an annual average of ~8 m/s in comparison to ~7 m/s from their Southern Hemisphere counterparts. The year-round north Pacific trade winds stretch across the entire ocean immediately south of Hawaii. The north Atlantic trade winds start offshore of Morocco and extend to the Caribbean. The Southern Hemisphere trade winds are the strongest in the Pacific extending from Chile-Peru to the mid ocean around 220°E. The resulting waves from these trade wind systems are relatively small compared to the waves generated by the Westerlies. The most prominent wave feature related to the trade winds is located in the north Pacific near Hawaii. The inter-tropical convergence zone (ITCZ), which separates the Northern and Southern Hemisphere trade wind regions, is seen to move north in JJA and south in DJF.

The Indian Ocean and the South China Sea have a very unique two-season pattern related to the monsoon in contrast to the Pacific and Atlantic Oceans. The wet season occurs in JJA with southerly winds across the region. The south Indian Ocean trades, which stretch from Western Australia to Madagascar, strengthen and migrate towards the Equator. Wind and wave activities intensify in the Arabian Sea and Bay of Bengal. The wave field in the region, with the exception in the Arabian Sea, is dominated by swells from extratropical storms off Antarctica. In the dry season during DJF, the Indian Ocean is calmer and the wind and wave directions reverse. The South China Sea becomes active. Persistent northeast winds extend from the east China coast with increasing speed toward the south. Increased wave activities start in the northern portion of the South China Sea and then extend south toward Indonesia. The winds near the Equator remain relatively calm throughout the year in this region.

General statistics of the wind and wave fields provide an overview of the dataset and insights into the extreme events. Fig. 4 displays the 50, 70, 80, 90, 95, and 99th percentile wind speed. The most prominent feature is the zonal structure, which includes the Westerlies, the trade wind regions, and the relatively calm regions centered within 8° from the Equator. In the Northern Hemisphere, the 50, 70, and 80th percentile have weaker wind speeds than those of the Southern Hemisphere, but the 90, 95, and 99th percentiles have similar magnitude. This is associated with the seasonal extremes in the Northern Hemisphere in DJF and JJA versus the year-round storm activities in the Southern Hemisphere as pointed out by Young (1999) and Izaguirre et al. (2011). Peaks in the wind field are seen in the north Pacific and north Atlantic most notably in the 99th percentile centered at 170°E 40°N and 320°E 55°N respectively. The Westerlies in the Southern Hemisphere have less identifiable peaks and are more spatially homogenous due to unimpeded wind flows. The land-sea boundary along Antarctica has strong temperature gradients that can produce very large wind speeds locally.

The percentile plots of the wave field in Fig. 5 show a similar pattern as the wind speed. The zonal structure is evident in the

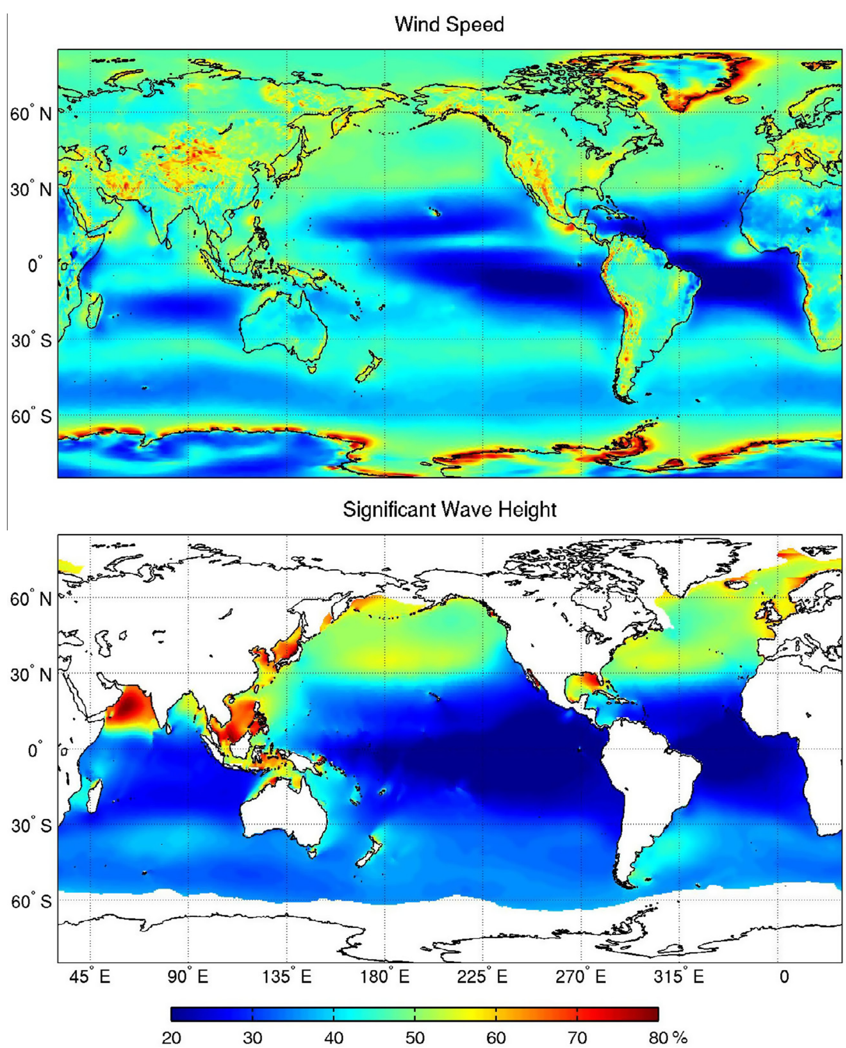

Fig. 6. Mean annual variability for wind speed (top) and significant wave height (bottom).

wave field as found by Vinoth and Young (2011) and Izaguirre et al. (2011) based on altimetry data. In the 50–95th percentiles, the Southern Hemisphere oceans have larger wave heights than their northern counterparts. However, the wave heights are comparable in both hemispheres in the 99th percentile. The most active region lies along 50°S known as the "roaring fifties". The wave height along this band peaks near Iles Kerguelen Island at approximately 70°E 50°S and extends toward Western Australia. In the Northern Hemisphere, the maxima occur in the center of the Pacific and in the Eastern Atlantic at 190°E 40°N and 345°E 55°N respectively. Some effects of the obstructions file used in WW3 can be seen in the south Pacific due to the large number of islands and atolls. The extremes from the CFSR winds and hindcast waves are qualitatively comparable to the altimetry data compiled by Vinoth and Young (2011) and Izaguirre et al. (2011).

5. Annual and inter-annual variability

The mean annual variability measures the spread of the data to provide an indication of the seasonal extremes. Let x denote the time series of wind speed or wave height over a period of m years with n records each. The mean annual variability (MAV), which is the average of the annual standard deviation normalized by the annual average, provides a measure of the variability within each year as

$$\mathrm{MAV} = \frac{1}{m}\sum_{j=1}^{m}\sqrt{\frac{1}{n}\sum_{k=1}^{n}\left(x_{jk} - \left(\frac{1}{n}\sum_{k=1}^{n}x_{jk}\right)\right)^2}\left(\frac{1}{n}\sum_{k=1}^{n}x_{jk}\right)^{-1} = \overline{\left(\frac{\sigma_j}{\overline{x_j}}\right)} \tag{1}$$

where the indices j and k refer to the year and record, σ is the standard deviation, and the over bar denotes average. Fig. 6 plots the MAV for the wind speed and wave height. A land and ice mask was used with the wave data because the intermittent ice coverage has resulted in the largest variability that obscures this metric particularly in the Southern Ocean.

The MAV shows the greatest variability within each year in the north Atlantic and north Pacific. The wind variability is approximately 50% along 40°N and is caused by the calm JJA and the extra-tropical storms in DJF. The wave variability is slightly higher at 60% along 40°N. The trade wind regions are rather constant with less than 20 percent variability for both the winds and waves. Strips of increased wind variability extend from Central America across the Pacific and from west Africa across the Atlantic along 10°N. These regions represent the furthest extent of the ITCZ movement and have 40–50% variability throughout the year in comparison to 20% in the trade wind regions immediately north and south. This fluctuation is not reflected in the waves, which have rather low variability in these regions. In general, the waves in the tropics from 25°S to 25°N are relatively constant throughout the year with

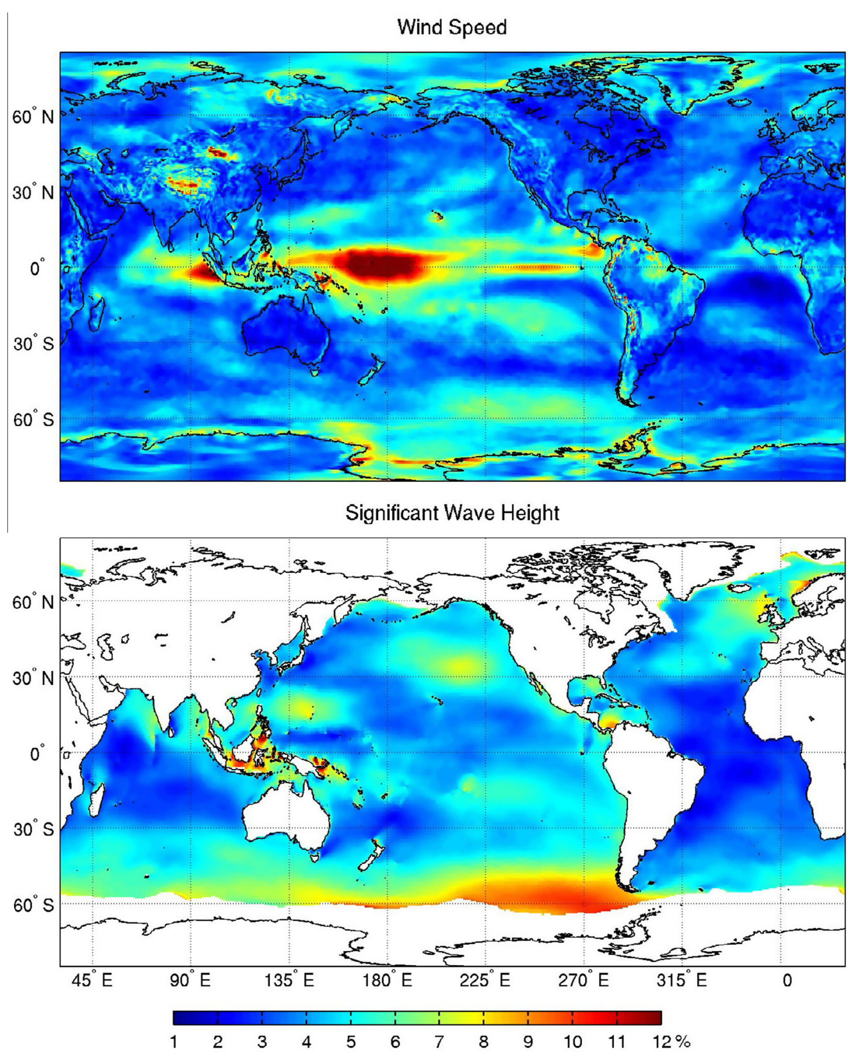

Fig. 7. Inter-annual variability for wind speed (top) and significant wave height (bottom).

less than 20% MAV. The Southern Hemisphere seasonal averages in Fig. 2 have shown the Westerlies strengthen and extend further north in JJA. This gives rise to an increase of the wind speed variability from 35% at 50°S to 50% at 40°S. The variability of the waves is less drastic in this region and is consistently in the range of 30% throughout the year due to the presence of swell. The air-sea interface acts as a filter and small-scale wind variations have subtle effects on the wave height in the open ocean. In addition, a significant portion of the wave energy is contained in the swell field that provides the background energy to moderate fluctuations associated with the winds in this portion of the Southern Ocean (Alves 2006; Semedo et al. 2011; Arinaga and Cheung, 2012).

The 0.5° resolution and 3-h time intervals in the CFSR data products reveal more refined features not obvious in previous global reanalysis datasets. The seasonal averages have demonstrated the linkage between the Arabian Sea and South China Sea in terms of wind and wave activities. The MAV clearly shows the large seasonal variability in these areas upward of 65% for the winds and 90% for the waves. Across the ocean, the winds show some effects of tropical cyclones in the storm generation areas to the west of Central America and west Africa. These areas are relatively calm with seasonal average wind speed of 6–8 m/s as shown in Fig. 2, but when a tropical disturbance is formed the winds can drastically exceed this level and accounts for the greater MAV. The variability in the waves is not observed most likely due to the consistent swells from the Northern and Southern Hemispheres that overshadow the tropical cyclone waves at their initial stage of development. The wind speed variation has much stronger effects in semi-enclosed seas such as the Caribbean Sea, the Yellow Sea, and the Sea of Japan, where the regions are sheltered from distant swells and respond more spontaneously to local wave generation.

The 31 years of data allow a systematic examination of the variability from year to year. The inter-annual variability (IAV) is defined as the standard deviation of the annual means normalized by the overall mean as

$$\mathrm{IAV} = \sqrt{\frac{1}{m}\sum_{j=1}^{m}\left[\left(\frac{1}{n}\sum_{k=1}^{n}x_{jk}\right)-\left(\frac{1}{m}\sum_{j=1}^{m}\left(\frac{1}{n}\sum_{k=1}^{n}x_{jk}\right)\right)\right]^2}\left(\frac{1}{nm}\sum_{j=1}^{m}\sum_{k=1}^{n}x_{jk}\right)^{-1} = \frac{\sigma_{\overline{x_j}}}{\overline{x}} \tag{2}$$

Fig. 7 shows the IAV for the winds and waves. The strongest signal in the winds is along the Equator from the Galapagos Islands to Eastern Indonesia with a maximum of 14% in the Western Pacific. The trade winds also exhibit some variability across the Pacific in both hemispheres. The Western Pacific has 8% variability associated with the trade winds, while the South Pacific has a similar level of variability, but the extent is much larger covering a region from Easter Island to French Polynesia. These features likely correspond to the ENSO, which is characterized by weakening of the easterly trade winds with a 2–5 year cycle. The ENSO signal might well account for the large variability offshore of Sumatra in the Indian Ocean. Another prominent feature is in the tropical cyclone generating regions of the Eastern Atlantic and Eastern Pacific varying 7–9% from year to year. Lastly, the Southern Ocean at 50°S has 8% variability from year to year that may be related to the AAO or the inter-annual variability of its extent.

The inter-annual variability of the wave field is quite different from the signals in the winds. The trade wind waves show considerable variability associated with the ENSO, but the strong variability in the wind field is not carried over to the waves along the Equator, which is typically not a wave generation region. Exceptions are the semi-enclosed bodies of water in the Caribbean north of Colombia, Bismarck and Solomon Seas east of Papua New Guinea, and Java and Celebes Seas around Indonesia. The wave field in the trade wind region of the Western Pacific has significant variability from year to year matching the value in the winds (~8%). The northeast Atlantic has significant variability of up to 8% that may be related to the AO. The Indian Ocean has little variation from year to year, while the variability is strong in the surrounding regions such as the Arabian Sea, the Bay of Bengal, and the South China Sea. These small seas typically have limited wave heights and become sensitive to climate cycles especially when influenced by swells. The Southern Ocean shows considerable variability in the wave field. Bosserelle et al. (2011) obtained similar results for an area offshore of Western Australia using the ERA-40 dataset. The largest variability of 12% off South America is in the same area shown in the wind field associated with the AAO and probably the variability of ice coverage.

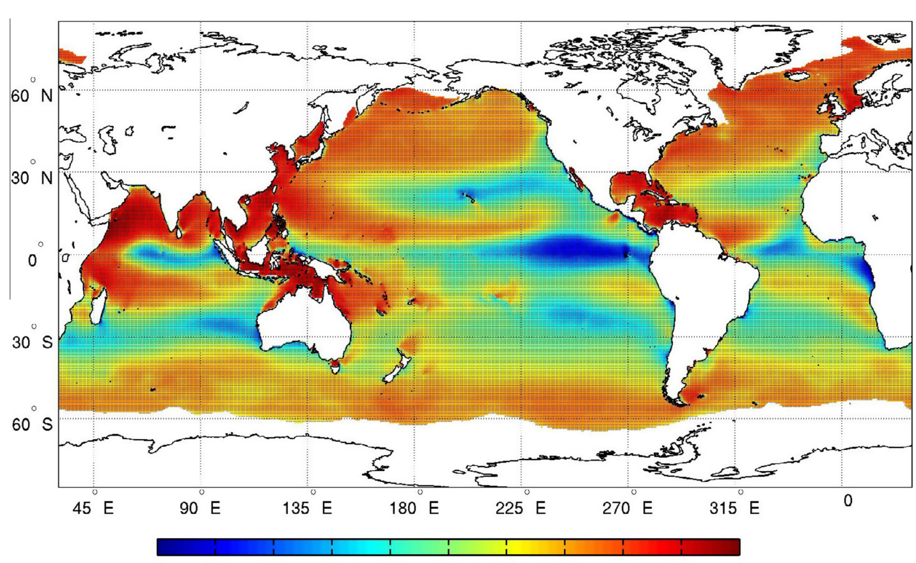

Fig. 8. Correlation between daily average wind speed and wave height. Shaded areas represent statistically significant results within 95%.

6. Correlation to climate cycles

The IAV and MAV hint that some of the variability in the winds and waves may be linked to atmospheric cycles. In this section, we examine the relationship between the wind and wave dataset as well as their correlation with the published indices of the AO, AAO, ENSO, and MJO in Section 2. Let x_i and y_i denote two time series with n records each. The correlation coefficient is defined as

$$r = \frac{\sum_{i=1}^{n}(x_i - \overline{x})(y_i - \overline{y})}{\sqrt{\sum_{i=1}^{n}(x_i - \overline{x})^2}\sqrt{\sum_{i=1}^{n}(y_i - \overline{y})^2}} = \frac{\mathrm{cov}(x, y)}{\sigma_x \sigma_y} \quad (3)$$

where cov(x,y) is the covariance and σ_x and σ_y are the standard deviations of the respective signals. The coefficient has a range of $-1 \leqslant r \leqslant 1$ indicating negative to positive correlation between the two time series. It determines how well the CFSR data products capture the cycles and complement previous studies by providing a global perspective (Wang and Swail 2001; Dodet et al., 2010; Hemer et al., 2010; Izaguirre et al., 2011; Semedo et al., 2011; Fan et al., 2012).

It is important to examine the relationship between the wind and wave datasets before assessing their correlation with the climate cycles. Fig. 8 plots the correlation coefficient between wind speed and wave height. Semi-enclosed seas like the South China Sea, Caribbean Sea, Sea of Japan, and Arabian Sea have the highest correlation between wind and wave conditions, because these regions are sheltered from distant swells and are dominated by wind waves locally. The wave-generating Westerlies regions also show strong correlation, but the adjacent areas have low values due to the presence of swells (Young, 1999; Alves, 2006; Semedo et al., 2011). The trade wind regions have a higher correlation coefficient down fetch in the western portion of the ocean associated with wave growth. The Equatorial regions have the lowest correlation coefficient. The areas in the low latitudes have waves from both hemispheres. The local winds, which are relatively weak, do not contribute much energy to the overall wave spectrum. The spatial distribution of the correlation coefficient in Fig. 8 allows us to interpret and distinguish the relative influence of the climate cycles between the winds and waves.

The climate cycles are known to influence the extremes more than the average weather conditions (Bacon and Carter, 1991; Wang and Swail 2001; Graham and Diaz, 2001; Woolf et al., 2002; Dodet et al., 2010; Hemer et al., 2010; Bosserelle et al., 2011; Izaguirre et al., 2011). The monthly averages of the highest 10% wind speed and wave height provide an indication of the more extreme events, while the monthly records above the 90th percentile of the entire time series provide a measure of their occurrences. Fig. 9 plots the correlation coefficients of these measures with the monthly AO index as well as the statistically significant regions over 95%. The index represents the strength of the Arctic circulation around 60°N. When the index is positive, there is an increase in the circulation with the jet stream shifted northward. The north Atlantic has the strongest correlation as expected and the results are statistically significant. Positive correlation of intensity and occurrence prevails from offshore of Greenland to the Scandinavian Peninsula. Conversely, the mid-latitude region in 30–50°N shows negative correlation. The occurrence shows stronger negative correlation than the intensity meaning that events occur more often with only moderate increase in wind speed and wave height. The trade winds of both the Atlantic and Pacific are positively correlated; however the waves are not statistically significant because

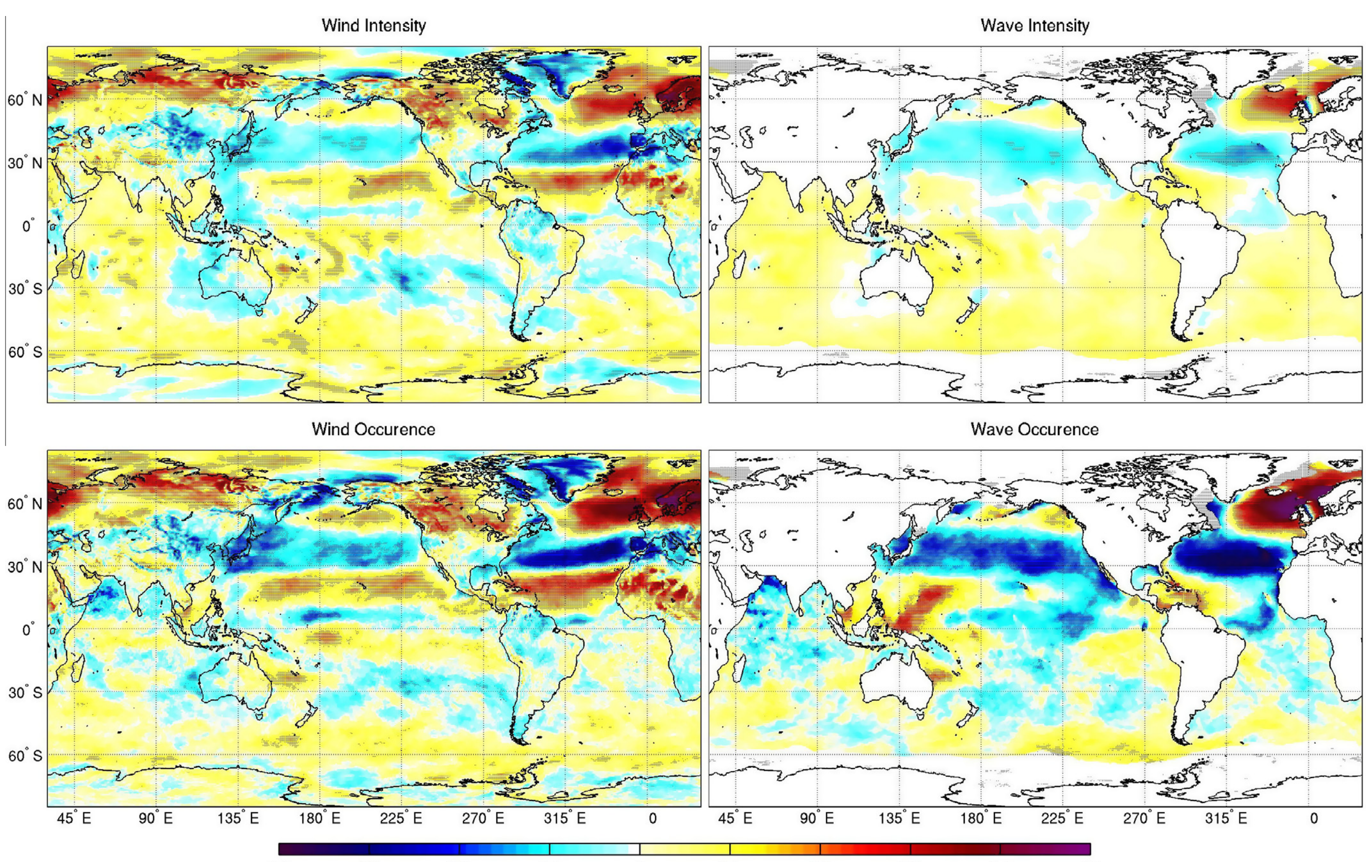

Fig. 9. Correlation of wind speed (left panels) and significant wave height (right panels) with the AO index. Shaded areas represent statistically significant results within 95%. The top and bottom panels show intensity and occurrence respectively.

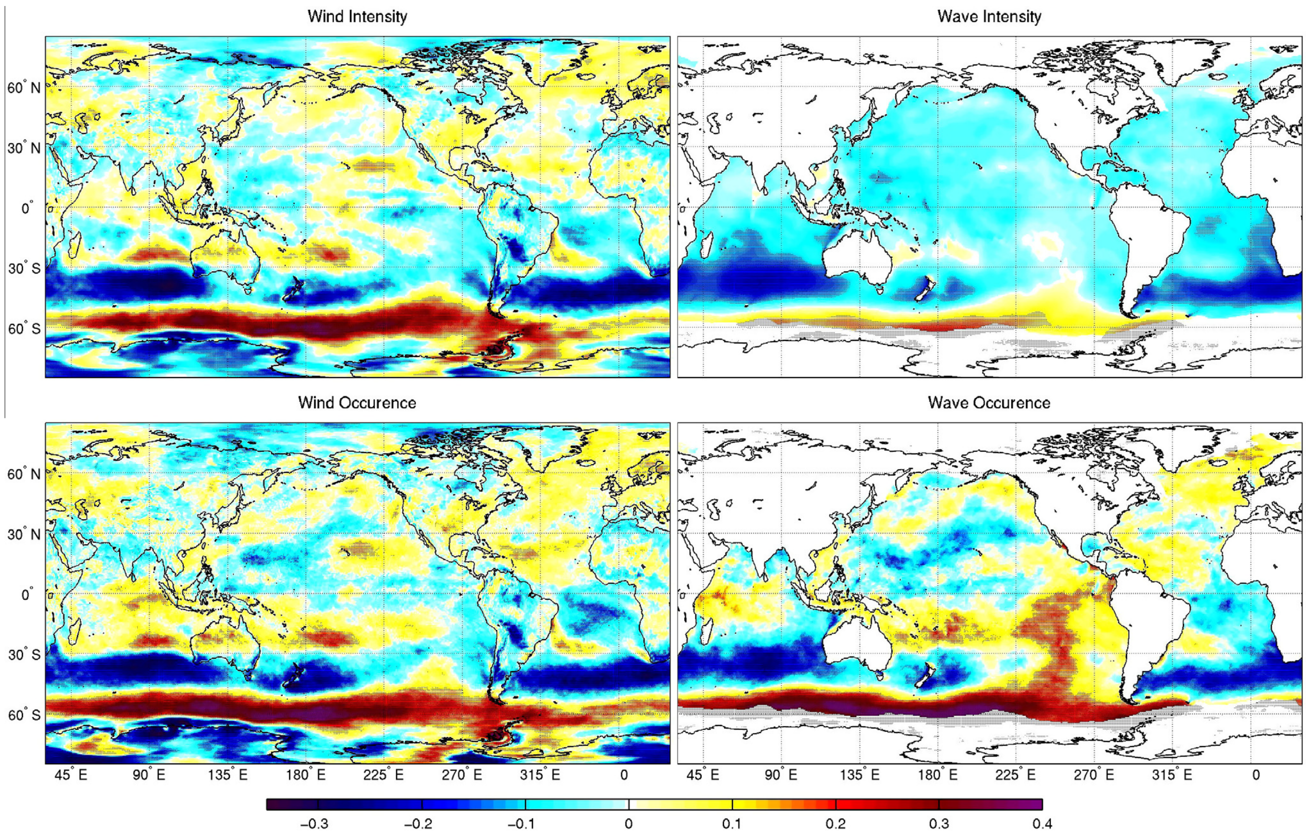

Fig. 10. Correlation of wind speed (left panels) and significant wave height (right panels) with the AAO index. Shaded areas represent statistically significant results within 95%. The top and bottom panels show intensity and occurrence respectively.

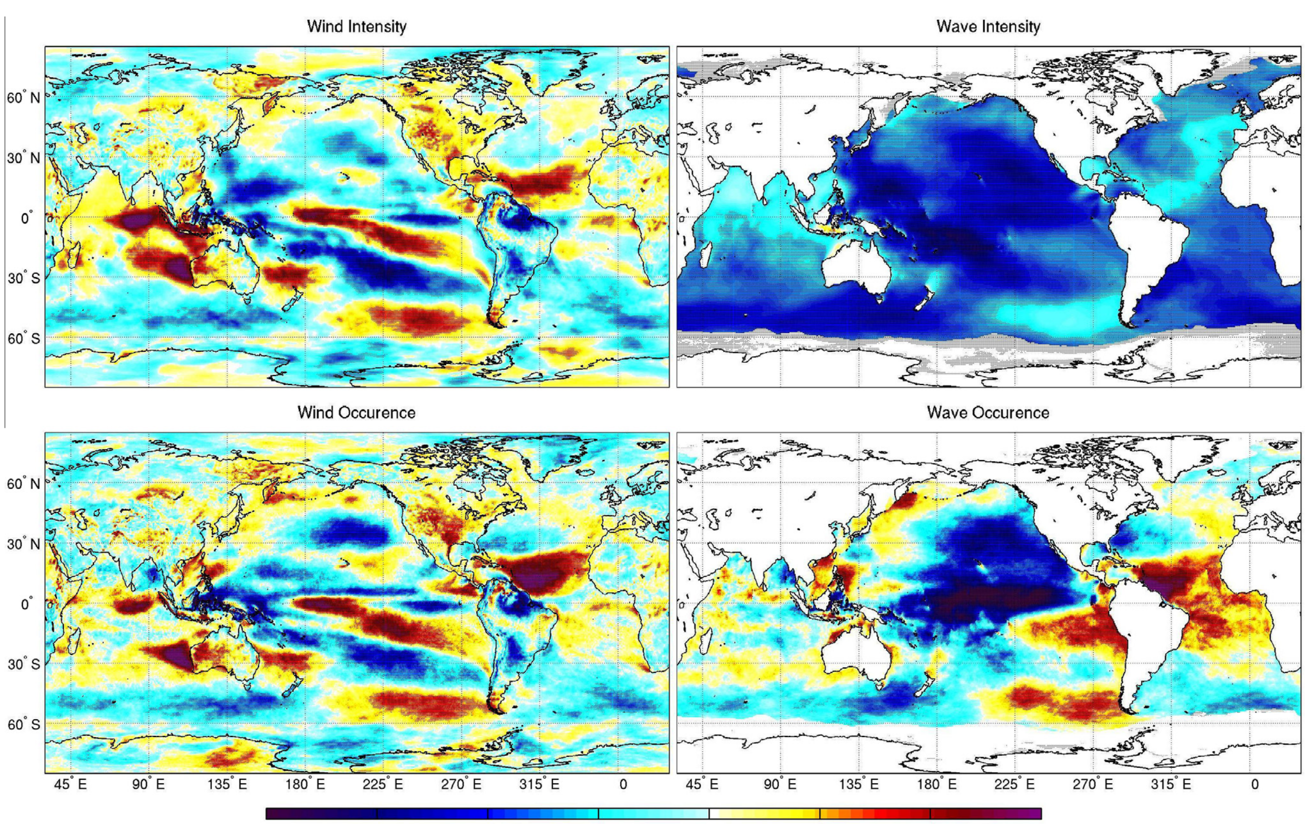

Fig. 11. Correlation of wind speed (left panels) and significant wave height (right panels) with the SOI. Shaded areas represent statistically significant results within 95%. The top and bottom panels show intensity and occurrence respectively.

of weak correlation between the winds and waves in the region. This pattern is consistent with the regression and extremal analysis of altimetry data by Woolf et al. (2002) and Izaguirre et al. (2011) as the well as the EOF, correlation, and regression analysis of numerically generated data by Wang and Swail (2001), Dodet et al. (2010), and Fan et al. (2012) respectively.

The intensity and occurrence of extremes are correlated to the AAO index in Fig. 10. When the index is positive, the polar circulation strengthens and moves toward Antarctica and vice versa. The intensity and occurrence show strong positive correlation with the index along 60°S. This corresponds to a shift of the Westerlies southward as the polar circulation intensifies. When the index is negative, the polar circulation relaxes and consequently the Westerlies shift northward. This increases the intensity and occurrence resulting in negative correlation in the lower latitudes. These zonal patterns are clearly seen in both the winds and waves. The AAO greatly affects the climate in Western Australia and modulates the storm tracks (Bosserelle et al., 2011). There is positive correlation between the trade winds offshore of Western Australia and northeast of New Zealand, but not as positively correlated in the wave field because of domination of swells in these regions. The waves show an interesting structure in the Eastern South Pacific that is not seen in the winds. There is positive correlation of occurrence that extends from 60°S to the Equator. When the index is positive, storms passing south of New Zealand have a wider fetch and generate swells that spread across the ocean towards the Americas. As the waves approach the Eastern Pacific they spread over a large region to reach the lower latitudes producing positive correlation. In general, both the winds and waves have a correlation coefficient of 0.4 in areas of significance. Hemer et al. (2010) found similar patterns and magnitude of the correlation coefficient in the Southern Hemisphere utilizing altimetry data from 1991 to 2006.

The SOI is an indicator of the ENSO, which is known to affect the tropics with effects across the globe. Fig. 11 compares its signals with the wind and wave data. The blue and red areas from the wind data denote negative and positive correlation associated with El Nino and La Nina. The most prominent features linked to El Nino are strengthening of weather systems in the Pacific. These include the winds along the Equator in the Eastern Pacific, the Easterly trade winds in the Southern Hemisphere extending past 30°S, the Western Pacific trade winds in the Northern Hemisphere, and the extratropical storms to the north of Hawaii. The areas associated with La Nina are the trade wind regions in the South Pacific extending to the Equator, the North Atlantic from West Africa to the Caribbean, and the Indian Ocean as well as the extratropical storm region in the Southern Ocean centered at 250°E 50°S. The correlation of the index with the waves shows different patterns. The statistically significant areas of the intensity show correlation with El Nino across the majority of the globe. The correlation of the

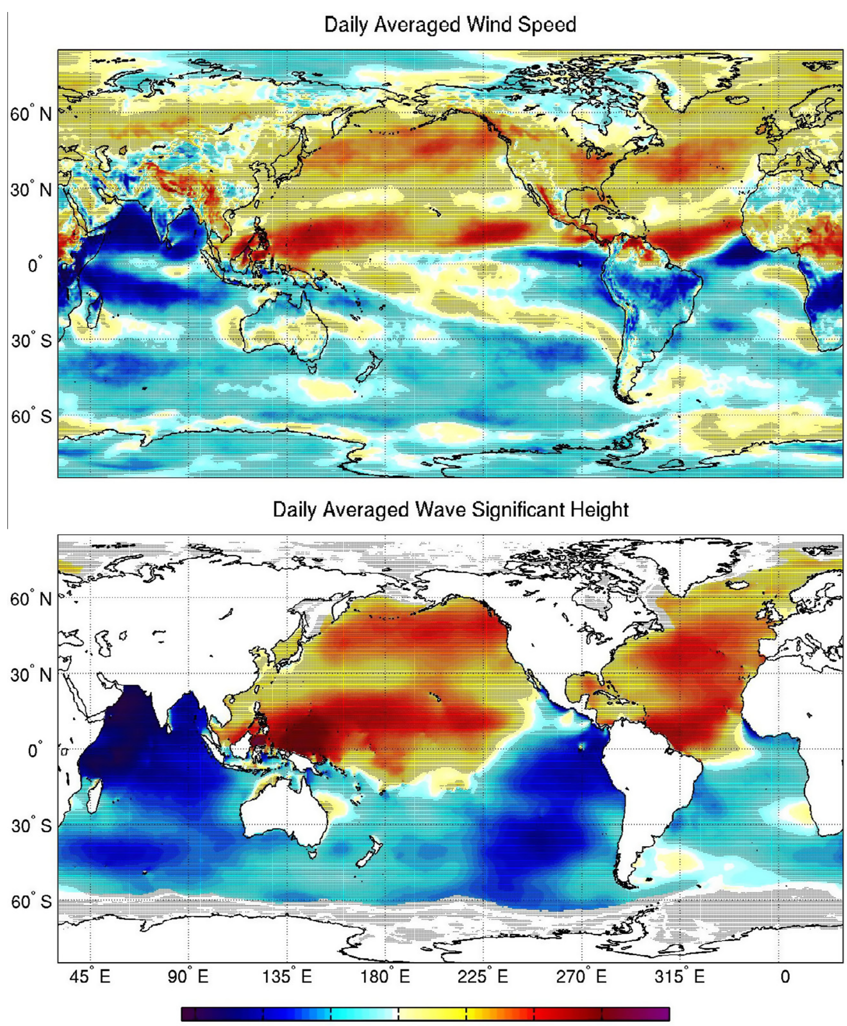

Fig. 12. Correlation of wind speed (top panel) and significant wave height (bottom panel) with the MJO index. Shaded areas represent statistically significant results within 95%.

occurrence is strong in the central and north Pacific, but weaker in the roaring fifties across most of the Southern Ocean. In particular, severe waves occur more frequently in the Equatorial region of the Pacific during El Nino years. The altimetry data of Hemer et al. (2010) and numerically generated data of Fan et al. (2012) also show strong influence of the El Nino in these regions. The La Nina phase is less prevalent in the wave height, but is characterized by increased wave occurrence in the trade wind regions of the north and south Atlantic, offshore of Peru, the South China Sea, and in the south Pacific offshore of Chile similarly reported by Izaguirre et al. (2011).

The MJO affects the same region as the ENSO but with a much smaller time scale. Weaver et al. (2011) showed that the CFSR (v1) captures effects of the MJO and its linkage to the ENSO. In the Western Pacific, the intensity of the MJO index increases in El Nino years and decreases in La Nina years. The oscillation starts in the Indian Ocean and propagates along the Equator of the Pacific and into the Atlantic every 30–90 days (Wheeler and Hendon, 2004). As such, daily averages of wind speeds and waves are compared to the MJO index and the corresponding correlation coefficients are plotted in Fig. 12. The wind speed shows strong negative correlation with the MJO across the Indian Ocean. The correlation coefficient, which becomes stronger and positive after the signal crosses into the South China Sea, modulates along the trade wind regions in the North Pacific and North Atlantic. A similar feature is seen in the Southern Hemisphere trade wind region starting in Indonesia and extending southeast to Chile. The influence of the MJO extends to the Westerlies in the Northern and Southern Hemispheres with positive and negative correlation respectively. This has been called the "Pineapple" express in the Northern Pacific as storms are steered north of Hawaii linking the pattern of tropical rainfall in the Western Pacific to increased precipitation in the Pacific Northwest (Higgins et al., 2000). The influence of MJO is filtered in the wave patterns, which still maintain negative correlation in the Indian Ocean and most of the Southern Hemisphere and positive in the Northern Hemisphere.

7. Conclusions

The CFSR wind and WW3 generated wave datasets provide a wealth of information for examination and interpretation of climate characteristics. The high resolution of 0.5° reveals large and small scale features over a continuous 31-year period for studies of the seasonal patterns as well as long-term climate cycles. Seasonal averages and percentiles reveal the overall features of the global wind and wave climate with strong zonal structures. The Northern Hemisphere has stronger seasonal patterns, while the Southern Hemisphere is more consistent throughout the year. The Indian Ocean has a two-season pattern with strong influences in the Arabian Sea and the South China Sea. The mean annual variability, which reveals regions with the largest seasonality, is as high as 70% for the winds in the Northern Hemisphere and lower than 30% in the tropics near the Equator. The waves have the largest variability in the Northern Hemisphere and in semi-enclosed basins sheltered from distant swells such as the Arabian Sea, South China Sea, and the Caribbean Sea. The inter-annual variability, which describes the year-to-year pattern, reveals some effects of long-period oscillations such as the AO, AAO, and ENSO. In particular, effects of the ENSO are clearly seen in the wind field near the Equator as well as selected areas of trade wind regions. The maximum variability in the wave field occurs in the Southeastern Pacific offshore of Chile.

Monthly averages and counts of the upper 10% wind speeds and wave heights, which are indicative of intensity and occurrence of extremes, show strong correlation to the AO, AAO, and SOI indices. The AO and AAO indices respectively measure the strength of the Arctic and Antarctic circumpolar jets at 60°. Positive correlation corresponds to shifting of extratropical storms to higher latitudes and strengthening of the circumpolar jets and trade winds in the respective hemisphere and vice versa. Correlation coefficients of 0.4 or higher are found in the statistically significant regions indicating the strong and clear AO and AAO signals in the datasets. The SOI comparison also reveals many statistically significant features associated with El Nino and La Nina. The El Nino phase shows intensification of extratropical storms in the north Pacific and selected regions in the Southern Ocean as well as trade winds in the south Pacific and Western Pacific, while La Nina enhances the trade winds in the Pacific Equatorial region and the Atlantic and extratropical storms in the Southeastern Pacific. The MJO, which occurs in the tropic regions with linkage to the ENSO, has distinct correlation with the wind field. It shows positive correlation in the Northern Hemisphere and negative in the Indian Ocean and the Southern Hemisphere. The climate cycles show strong influences on the storm pattern, but their effects on the wave pattern are filtered and diffused through the air-sea interface.

Acknowledgement

The Department of Energy supported this study through Grant No. DE-FG36-08G018180 via the National Marine Renewable Energy Center. We would like to thank the guest editor Dr. Mark Hemer, Dr. Fernando Mendez, and two anonymous reviewers for the comments and suggestions that have improved this paper. SOEST Contribution Number 8699.

References

Alexander, M.A., Blade, I., Newman, M., Lanzante, J.R., Lau, N.C., Scott, J.D., 2002. The atmospheric bridge: the influence of ENSO teleconnections on air-sea interaction over the global oceans. Journal of Climate 15 (16), 2205–2231.

Alves, J.-H.G.M., 2006. Numerical modeling of ocean swell contributions to the global wind-wave climate. Ocean Modelling 11 (1–2), 98–122.

Arinaga, R.A., Cheung, K.F., 2012. Atlas of global wave energy from 10 years of reanalysis and hindcast data. Renewable Energy 39 (1), 49–64.

Bacon, S., Carter, D.J.T., 1991. Wave climate changes in the north Atlantic and north sea. International Journal of Climatology 11 (5), 545–558.

Bosserelle, C., Pattiaratchi, C., Haigh, I., 2011. Inter-annual variability and longer-term changes in the wave climate of Western Australia between 1970 and 2009. Ocean Dynamics 61 (1), 63–76.

Bromirski, P.D., Cayan, D.R., Flick, R.E., 2005. Wave spectral energy variability in the northeast Pacific. Journal of Geophysical Research 110(C0), 3005, http://dx.doi.org/10.1029/2004JC002398.

Caires, S., Sterl, A., Bidlot, J.-R., Graham, N., Swail, V., 2004. Intercomparison of different wind-wave reanalysis. Journal of Climate 17 (10), 1893–1913.

Chawla, A., Tolman, H.L., 2008. Obstruction grids for spectral wave models. Ocean Modelling 22 (1), 12–25.

Chawla, A., Spindler, D.M., Tolman H.L., 2013. Validation of a thirty year wave hindcast using the climate forecast system reanalysis winds. Ocean Modell. 70, 189–206.

Chen, G., Chapron, B., Ezraty, R., Vandemark, D., 2002. A global view of swell and wind sea climate in the ocean by satellite altimeter and scatterometer. Journal of Atmospheric Oceanic Technology 19 (11), 1849–1859.

Dee, D.P., Uppala, S.M., Simmons, A.J., coauthors, 2011. The ERA-Interim reanalysis: configuration and performance of the data assimilation system. Quarterly Journal of the Royal Meteorological Society, 137(656), 553–597.

Dodet, G., Bertin, X., Taborda, R., 2010. Wave climate variability in the North-East Atlantic Ocean over the last six decades. Ocean Modelling 31 (3–4), 120–131.

Ek, M.B., Mitchell, K.E., Lin, Y., Rogers, E., Grunmann, P., Koren, V., Gayno, G., Tarplay J.D., 2003. Implementation of Noah land surface model advances in the National Centers for Environmental Prediction operational mesoscale Eta model. Journal of Geophysical Research 108(D22), 10.1029/2002JD003296.

Fan, Y., Lin, S.-J., Held, I.M., Yu, Z., Tolman, H.L., 2012. Global ocean surface wave simulation using a coupled atmosphere-wave model. Journal of Climate 25 (18), 6233–6252.

Graham, N.E., Diaz, H.F., 2001. Evidence for intensification of North Pacific winter cyclones since 1948. Bulletin of American Meteorological Society 82 (9), 1869–1893.

Genmrich, J., Thomas, B., Bouchard, R., 2011. Observational changes and trends in the northeast Pacific wave records. Geophysical Research Letters 38, L22601. http://dx.doi.org/10.1029/2011GL049518.

Gulev, S.K., Grigorieva, V., 2006. Variability of the winter wind waves and swell in the North Atlantic and North Pacific as revealed by voluntary observing ship data. American Meteorological Society 19 (21), 5667–5685.
Gulev, S.K., Grigorieva, V., Sterl, A., Woolf, D., 2003. Assessment of the reliability of wave observations from voluntary observing ships: Insights from the validation of a global wind wave climatology based on voluntary observing ship data. Journal of Geophysical Research 108(C1), 3236, doi:10.1029/2002JC001437.
Hemer, M.A., Church, J.A., Hunter, J.R., 2010. Variability and trends in the directional wave climate of the Southern Hemisphere. International Journal of Climatology 30 (4), 475–491.
Higgins, R.W., Schemm, J.K.E., Shi, W., Leetmaa, A., 2000. Extreme precipitation events in the western United States related to tropical forcing. Journal of Climate 13 (4), 793–820.
Izaguirre, C., Mendez, F.J., Menendez, M., Losada, I.J., 2011. Global extreme wave height variability based on satellite data. Geophysical Research Letters 38, L10607. http://dx.doi.org/10.1029/2011GL047302.
Kalnay, E., Kanamitsu, M., Kistler, R., coauthors, 1996. The NCEP/NCAR 40-year reanalysis project. Bulletin of American Meteorological Society, 77(3), 437–471.
Kistler, R., Kalnay, E., Collins, W., coauthors, 2001. The NCEP-NCAR 50-year reanalysis: monthly means CD-ROM and documentation. Bulletin of American Meteorological Society, 82(2), 247–267.
Kleist, D.T., Parrish, D.F., Derber, J.C., Treadon, R., Errico, R.M., Yang, R., 2009. Improving incremental balance in the GSI 3DVAR analysis system. Monthly Weather Review 137 (3), 1046–1060.
Madden, R.A., Julian, P.R., 1972. Description of global-scale circulation cells in the Tropics with a 40–50 day period. Journal of Atmospheric Science 29 (10), 1109–1123.
Menendez, M., Mendez, F.J., Losada, I.J., Graham, N.E., 2008. Variability of extreme wave heights in the northeast Pacific Ocean based on buoy measurements. Geophysical Research Letters 35, L22607. http://dx.doi.org/10.1029/2008GL035394.
Reguero, B.G., Menendez, M., Mendez, F.J., Minguez, R., Losada, I.J., 2012. A global ocean wave (GOW) calibrated reanalysis from 1948 onwards. Coastal Engineering 65, 38–55.
Saha, S., Moorthi, S., Pan, H.L., coauthors, 2010. The NCEP Climate Forecast System Reanalysis. Bulletin of the American Meteorological Society 91(8), 1015–1057.
Semedo, A., Suselij, K., Rutgersson, A., Sterl, A., 2011. A global view on the wind sea and swell climate and variability from ERA-40. Journal of Climate 24 (5), 1461–1479.
Sterl, A., Caires, S., 2005. Climatology, variability and extrema of ocean waves: the web-based KNMI/ERA-40 wave atlas. International Journal of Climatology 25 (22), 963–977.
Sterl, A., Komen, G.J., Cotton, D., 1998. 15 years of global wave hindcasts using ERA winds: Validating the reanalyzed winds and assessing the wave climate. Journal of Geophysical Research 103(C3), 5477–5492.
Thompson, D.W.J., Wallace, J.M., 1998. The Arctic Oscillation signature in the wintertime geopotential height and temperature fields. Geophysical Research Letters 25 (5), 1297–1300.
Tolman, H.L., Chalikov, D.V., 1996. Source terms in a third-generation wind-wave model. Journal of Physical Oceanography 26 (11), 2497–2518.
Tolman, H.L., Balasubramaniyan, B., Burroughs, L.D., Chalikov, D.V., Chao, Y.Y., Chen, H.S., Gerald, V.M., 2002. Development and implementation of wind generated ocean surface wave models at NCEP. Weather and Forecasting 17 (2), 311–333.
Tolman, H.L., 2008. A mosaic approach to wind wave modeling. Ocean Modelling 25 (1–2), 34–47.
Tsai, C.P., Hwang, C.H., Hwa, C., Cheng, H.Y., 2012. Study on the wave climate variation to the renewable wave energy assessment. Renewable Energy 38 (1), 50–61.
Uppala, S.M., Kallberg, P.W., Simmons, A.J., coauthors, 2005. The ERA-40 Re-analysis. Quarterly Journal of the Royal Meteorological Society 131(612), 2961–3012.
Vinoth, J., Young, I.R., 2011. Global estimates of extreme wind speed and wave height. Journal of Climate 24 (6), 1647–1665.
Wallace, J.M., Gutzler, D.S., 1981. Teleconnections in the geopotential height field during the Northern Hemisphere winter. Monthly Weather Review 109 (4), 784–812.
Walker, G.T., Bliss, E.W., 1932. World Weather V. Memoirs of the Royal Meteorological Society 4 (36), 53–83.
Walker, G.T., Bliss, E.W., 1937. World Weather VI. Memoirs of the Royal Meteorological Society 4 (39), 119–139.
Wamdig, 1988. The WAM model – A third generation ocean wave prediction model. Journal of Physical Oceanography 18 (12), 1775–1810.
Wang, X.L., Swail, V.R., 2001. Changes of extreme wave heights in Northern Hemisphere Oceans and related atmospheric circulation regimes. Journal of Climate 14(10), 2204–2221.
Weaver, S.J., Wang, W.Q., Chen, M.Y., Kumar, A., 2011. Representation of MJO Variability in the NCEP climate forecast system. Journal of Climate 24 (17), 4676–4694.
Wheeler, M., Hendon, H., 2004. An all-season real-time multivariate MJO index: development of an index for monitoring and prediction. Monthly Weather Review 132 (8), 1917–1932.
Woolf, D.K., Challenor, P.G., Cotton, P.D., 2002. Variability and predictability of the North Atlantic wave climate. Journal of Geophysical Research 107(C10): 3145. http://dx.doi.org/10.1029/2001JC001124.
Wu, X., Moorthi, K.S., Okomoto, K., Pan H.L., 2005. Sea ice impacts on GFS forecasts at high latitudes, In: Preprints, Eighth Conference on Polar Meteorology and Oceanography, San Diego, CA, American Meteorological Society, 7.4.
Yang, F., Pan, H.L., Krueger, S.K., Moorthi, S., Lord, S.J., 2006. Evaluation of the NCEP global forecast system at the ARM SGP site. Monthly Weather Review 134 (12), 3668–3690.
Young, I.R., 1999. Seasonal variability of the global ocean wind and wave climate. International Journal of Climatology 19 (9), 931–950.
Young, I.R., Zieger, S., Babanin, A.V., 2011. Global trends in wind speed and wave height. Science 332 (6028), 451–455.